

# A 3D Network of Nanochannels for Possible Ion and Molecule Transit in Mineralizing Bone and Cartilage

Tengteng Tang, William Landis, Emeline Raguin, Peter Werner, Luca Bertinetti, Mason Dean, Wolfgang Wagermaier, and Peter Fratzl\*

During crucial growth stages of vertebrate long bones, calcified cartilage beneath the growth plate is anchored to bone by a third mineralized component, the cement line. Proper skeletal development is contingent on the interplay of these three constituents, yet their mineralization processes and structural interactions are incompletely understood, in part from limited knowledge of their meso- and nanoscale features. Herein, focused ion beam-scanning electron microscopy (FIB-SEM) with serial surface imaging is applied to examine the cartilage–bone interface of mouse femoral heads at an unprecedented scale: FIB-SEM provides 3D, nanometer resolution of structural details for volumes encompassing metaphyseal calcified cartilage, bone, and the intervening cement line. A novel and complex structural network is revealed, comprising densely packed nanochannels smaller than bone canaliculi ( $\approx 10\text{--}50$  nm diameter) within the calcified cartilage and bone extracellular matrices, but absent in the cement line. A structural correlation is demonstrated between the nanochannels and ellipsoidal mineral domains, which appear to coalesce during mineralization in a process analogous to powder sintering in metallurgy. A mineralization process is proposed, supported by energy-dispersive X-Ray spectroscopy of nanochannel contents, in which these unreported structures offer ion and molecule conduits to access the extracellular matrices of calcified cartilage and bone.


by osteoclasts and osteoblasts.<sup>[1]</sup> In these template regions, the endochondral ossification process results in several tissue type transitions, also producing an anatomical stratification of tissues with different structural and functional domains, interacting in close association: at the border of the unmineralized cartilage template, calcified cartilage is cemented to the underlying bone by an intervening layer, called the cement line.<sup>[2,3]</sup> While calcified cartilage, bone, and the cement line are all comprised of nanometer-sized mineral particles embedded in an extracellular matrix (ECM) of collagenous and noncollagenous molecules,<sup>[4]</sup> they are each dramatically different in their mechanical properties and ultrastructures.<sup>[4]</sup> Despite extensive previous studies,<sup>[5]</sup> the development of tissue ultrastructure and the fundamental mechanisms of cartilage, bone, and cement line mineralization (and how they may be different or similar) are not fully understood. In particular, compared to cartilage and bone, even the composition of the cement line remains unclear, although in osteonal bone

it is believed to be rich in the ECM protein, osteopontin.<sup>[6]</sup> There is a notable absence of detailed information concerning the respective meso- and nanoscale structural characteristics of the different tissue types where they adjoin. Importantly, no studies have examined the mineralization patterns across calcified cartilage, bone, and the cement line within the same tissue volume, which is critical for understanding how the tissues grow and connect to one another and are restructured during tissue transitions.

## 1. Introduction

Cartilage and bone are principal skeletal tissues that interact extensively throughout the vertebrate body. In mice and most vertebrate animals, a cartilage–bone interface is formed through endochondral ossification, in which a cartilaginous template becomes mineralized by means of vascular invasion and chondrocyte replacement and is then partially remodeled into bone

T. Tang, E. Raguin, P. Werner, W. Wagermaier, P. Fratzl  
Department of Biomaterials  
Max Planck Institute of Colloids and Interfaces  
Am Mühlenberg 1, 14476 Potsdam, Germany  
E-mail: Peter.Fratzl@mpikg.mpg.de

 The ORCID identification number(s) for the author(s) of this article can be found under <https://doi.org/10.1002/anbr.202100162>.

© 2022 The Authors. Advanced NanoBiomed Research published by Wiley-VCH GmbH. This is an open access article under the terms of the Creative Commons Attribution License, which permits use, distribution and reproduction in any medium, provided the original work is properly cited.

DOI: 10.1002/anbr.202100162

W. Landis  
Department of Preventive and Restorative Dental Sciences  
University of California at San Francisco  
707 Parnassus Avenue, San Francisco, CA 94143, USA

L. Bertinetti  
Center for Molecular Bioengineering  
TU Dresden  
Tatzberg 41, 01307 Dresden, Germany

M. Dean  
Department of Infectious Diseases and Public Health  
City University of Hong Kong  
31 To Yuen Street, Tat Chee Avenue, Kowloon, Hong Kong

A particularly important cartilage–bone interface is the growth plate region of vertebrate long bones, which plays a central role in normal long bone growth and skeletal development.<sup>[7]</sup> This interface also appears to be the site at which slipping of the capital femoral epiphysis occurs in adolescence, a serious human disorder that interrupts bone lengthening in affected individuals.<sup>[8]</sup> Because of the recognized importance of the cartilage–bone interface in normal and abnormal bone formation, the integration of cartilage and bone, two largely dissimilar tissues as noted above, to achieve optimum functionality has attracted increasing research interest in materials design, tissue engineering, and orthopedic research.<sup>[4]</sup> However, mimicking the biological and mechanical performance of the natural cartilage–bone interface has been extremely challenging, a difficulty attributed again to limited knowledge of the local mineralization processes and the nanostructural properties of the tissues and interfaces they produce.

Development of mineralized cartilage and bone is partially orchestrated by distinct tissue-forming cells: chondrocytes in cartilage and osteoblasts (later becoming osteocytes) in bone. Osteocytes reside in a complex 3D network, housed in lacunar cavities interconnected by passages (canaliculi,  $\approx 100\text{--}300\text{ nm}$  in diameter), containing dendritic cell extensions (cell processes), bone fluid, and macromolecular complexes.<sup>[9]</sup> Canaliculi play an essential role in cell–cell communication, bone mineral homeostasis, and mineralization.<sup>[9]</sup> Intracellular signaling is initiated by the cell processes within canaliculi<sup>[10]</sup> and canaliculi likely contribute to the transport of mineral precursors to the mineralization front.<sup>[11]</sup> In contrast to the extensive studies concerning interacting osteocyte networks in bone,<sup>[9–11]</sup> chondrocyte communication in cartilage, particularly mineralized cartilage, is much less understood. It is generally believed that chondrocytes are isolated in their respective lacunae and the cells communicate primarily through diffusion of molecules through their extracellular matrix.<sup>[12]</sup> However, more recently, Mayan et al.<sup>[13]</sup> have provided evidence that direct connections between neighboring articular chondrocytes through gap junctions might play a role in cell–cell communication, chondrocyte and cartilage metabolism, and other functions. The implication of such a study<sup>[13]</sup> is that investigations of nanoscale architecture could provide core functional perspectives into tissue physiology.

Recent advances in characterization techniques have allowed the interrogation of bone architecture at the meso- and nanoscale in 3D and provided new insight into fundamental mineralization mechanisms of this tissue. Using focused ion beam-scanning electron microscopy (FIB-SEM), for example, Buss et al.<sup>[14]</sup> reported that, at the mineralization front of mouse tibiae, ellipsoidal meso- and nanoscale mineralization foci within tissue collagen bundles grew to abut each other, forming a contiguous mineral tessellation pattern, associated with lamellar bone periodicity. Similar ellipsoidal mineral domains were also identified in human femoral bone using plasma FIB.<sup>[15]</sup> However, it was unclear how such focal mineral domains arose and developed during the bone mineralization process and whether they occurred in other mineralizing tissues such as calcified cartilage. The presence of such domains could indicate that they are fundamental and general building blocks in vertebrate tissue mineralization.

The present investigation utilizes FIB-SEM in serial surface view mode to provide an ultrastructural characterization of calcified cartilage, bone, and the cement line interface between

them in the proximal femoral metaphysis of BALB/c mice. This technique circumvents a major challenge in studying the cartilage–bone interface by allowing the examination of a tissue-relevant field of view (in the tens of micrometers) but at nanometer resolution in 3D of the various structures and tissues that converge at the cartilage–bone junction. With this approach, an extensive, but previously unknown 3D network of nanoscale channels has been demonstrated, permeating the cartilage and bone matrices, but absent from the intervening cement line. While the exact function of the channels remains incompletely determined, they tend to surround individual mineralization domains appearing similar to those reported at the bone mineralization front.<sup>[14,15]</sup> Such domains may undergo a maturation process that resembles the sintering of traditional materials.<sup>[16,17]</sup> Further energy-dispersive X-Ray spectroscopy (EDX) analysis found the channels filled with organic molecules, possibly containing phosphorus and calcium ions. The subcanalicular network demonstrated here in calcified cartilage and bone at the growth plate of long bones could therefore contribute to the development and coalescence of mineralization foci by supporting a pivotal function in passive and/or active transport of mineral ions and small molecular complexes to make them accessible to the collagenous extracellular matrices of these tissues. In revealing the presence of an extensive structural network common to different tissue types, the current work addresses the critical question of how ions necessary for mineralization are delivered deep into mineralizing tissues. The study also provides anatomical evidence for the proposal of a maturation route from apatite crystals to mineral domains involving a biological “sintering” process, analogous to one found in metallurgy.

## 2. Results and Discussion

### 2.1. Microstructural Features of the Mouse Femoral Head

The findings detailed below center on fine-scale relationships of mineralized cartilage and bone, which interface in different regions of the proximal mouse femur. As a preface to structural and analytical details obtained in this study, the following description provides a basic understanding of orientation and general morphology of the specimens investigated. Microcomputed tomography (micro-CT) of 9 week-old mouse femoral heads (**Figure 1A–C**) showed that their epiphyses principally contained calcified cartilage with a porous honeycomb appearance, a vastly different microstructure from that of the much denser trabecular bone of the metaphysis (**Figure 1C**). No subchondral bone plate was observed beneath the articular cartilage but, in some cases, regions of the epiphyseal calcified cartilage appeared to be replaced by bone tissue, as shown by the tissue ultrastructure (**Figure S1**, Supporting Information). Structural indications of partial replacement of cartilage by bone were also found at the growth plate where bony structures occasionally traversed the unmineralized growth plate (**Figure S1**, Supporting Information), an observation suggesting the onset of epiphyseal fusion. The finding that calcified cartilage can form in the mouse epiphysis without associated development of a secondary ossification center (including a subchondral bone plate and trabecular bone) was consistent with a previous report of

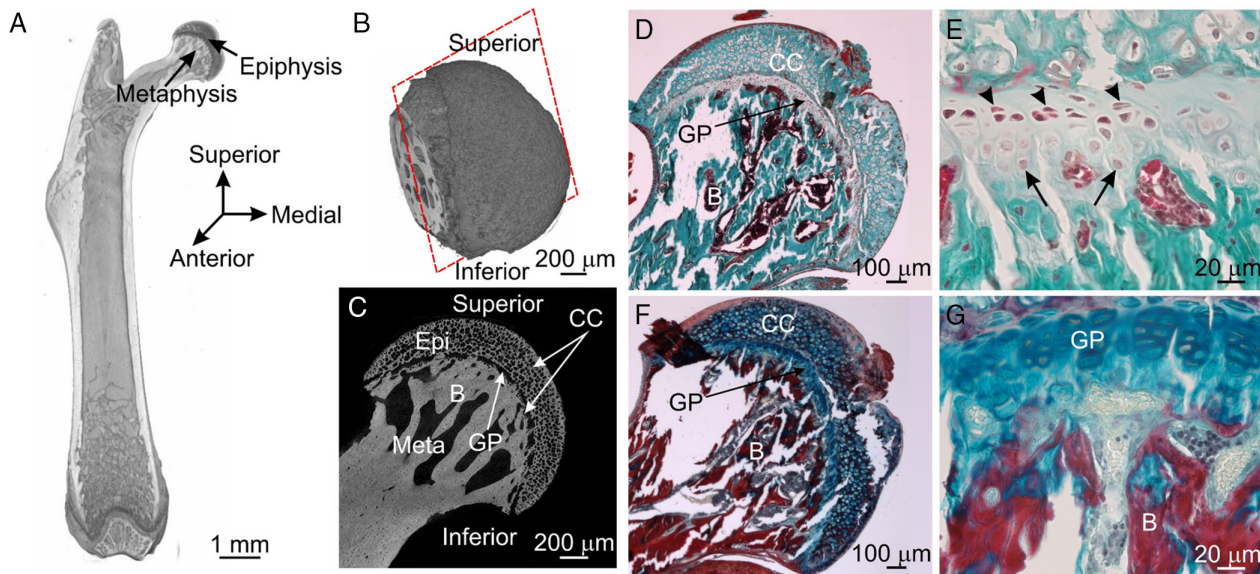


**Figure 1.** A–C) Micro-CT images of the proximal femur from a 9 week-old BALB/c mouse and D–G) optical microscopy images of representative tissue sections stained with Goldner's trichrome (D,E) and Alcian blue and Picrosirius red (F,G). (A) 3D reconstruction of the micro-CT data of the entire mouse femur viewed from the coronal plane. Arrows point to the epiphysis and metaphysis of the femoral head. A set of orthogonal coordinates defines the spatial orientation and anatomic location of the femur and its features. (B) Micro-CT reconstruction of the mouse femoral head illustrating the direction of sample sectioning taken in the coronal plane (dashed red frame) along the superior-to-inferior axis of the femoral head. (C) A representative high-resolution micro-CT image of the mouse femoral head showing calcified cartilage (CC) in the epiphysis (Epi), unmineralized growth plate cartilage (GP), and calcified cartilage (CC) and bone (B) in the metaphysis (Meta). (D) Goldner's trichrome staining of a representative undecalcified tissue section taken in the coronal plane following (C) and showing mineralized matrix (calcified cartilage, CC, and bone, B) and growth plate (GP, arrow). The growth plate is located between epiphyseal calcified cartilage and bone and may be identified by its lighter green stain compared to the darker green of calcified cartilage and bone. (E) Magnified image of growth plate cartilage and its individual chondrocytes (arrowheads and arrows). Chondrocytes are more flattened (arrowheads) in proximal regions of the growth plate and become hypertrophic (arrows) in distal regions. (F) An image of an Alcian blue- and Picrosirius red-stained sample section corresponding to (D) and revealing proteoglycans (blue) and collagen (red). Calcified cartilage (CC), growth plate (GP, arrow), and bone (B) are as marked. (G) Enlargement of an area of the growth plate and metaphysis in a section similar to that of (F) showing deeper blue staining and thus greater proteoglycan content in the growth plate (GP) region compared to that of metaphyseal bone (B), identified principally by its red staining of collagen.

mineralization in this tissue.<sup>[18]</sup> Goldner's trichrome staining revealed that the epiphysis consisted of an avascular cartilage matrix harboring chondrocytes (Figure 1D) and the growth plate was characterized by regions of resting (Figure 1E, arrowheads) and hypertrophic chondrocytes (Figure 1E, arrows) without discernible boundaries between the zones of proliferation and hypertrophy. Alcian blue and Picrosirius red staining were intense and widespread over the tissue, evidence demonstrating a relatively high proteoglycan content in the calcified cartilage and growth plate compared to metaphyseal bone (Figure 1F,G).

## 2.2. Nanochannels in the Matrices of Calcified Cartilage and Metaphyseal Bone

The metaphyseal interface of calcified cartilage and bone in the murine proximal femur model was selected for more detailed investigation, as it represents an important transitional area from the unmineralized growth plate to the underlying bone tissue (Figure 2A, ROI). Backscattered electron microscopy (BSE) imaging, a technique that is sensitive to the local mineral content of a sample,<sup>[19]</sup> was used to identify mineralized regions of interest (ROIs) over the specimen surface (coronal plane of the mouse femoral head) and showed a bright and seemingly highly mineralized cement line (CL) between metaphyseal calcified cartilage

(CC) and bone (B) (Figure 2B). To characterize ultrastructural features of metaphyseal calcified cartilage, the cement line, and metaphyseal bone, FIB-SEM imaging, a 3D volume imaging technique, can generate stacks of images at nanometer resolution. FIB-SEM was conducted with the imaging plane perpendicular to the cement line in the coronal plane and the milling direction approximately following the plane of the cement line (Figure 2B). Low-resolution FIB-SEM imaging revealed a complex lacunocanalicular network in bone, which stopped at the cement line (Figure S2 and Movie S1, Supporting Information), while the neighboring calcified cartilage was absent of any such network. However, upon close examination with high-resolution FIB-SEM imaging, numerous dark, fine pores far smaller than bone canaliculi ( $\approx 10\text{--}50$  nm in diameter) were found in both the calcified cartilage (Figure 2C,D) and bone compartments of the tissue (Figure 3A,B). In the two planes orthogonal to the imaging plane, these pores appeared as elongated dark lines (Figure 2C and 3A, arrowheads). On reconstruction of such structures in 3D (Figure 2E–G and 3C–E), an extensive network of small channels, termed nanochannels, was discovered in both calcified cartilage (Figure 2E–G and Movie S2, Supporting Information) and bone (Figure 3C–E and Movie S2, Supporting Information). When rendered in 3D, the nanochannels appeared to bifurcate (Figure 2G and 3D) and interconnect

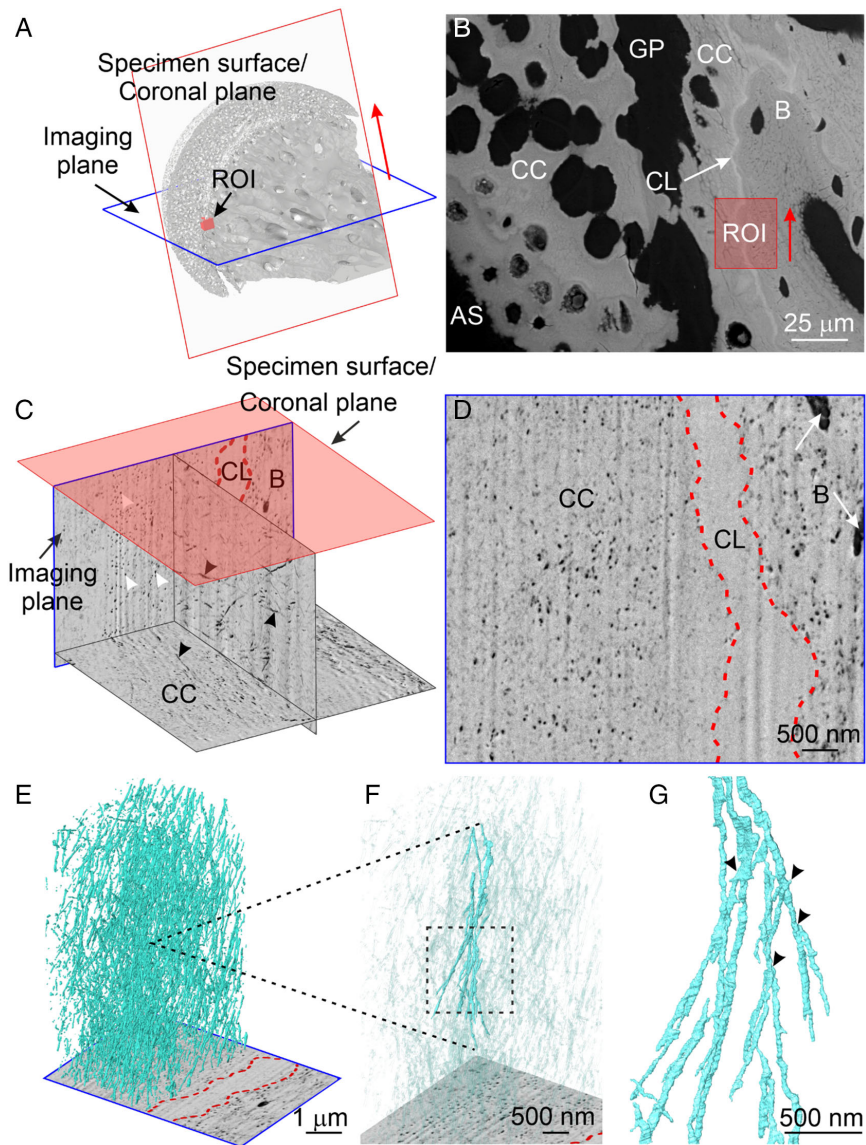


**Figure 2.** Examination of the interface between growth plate calcified cartilage and metaphyseal bone of a mouse femoral head. A) Micro-CT reconstruction of a 9 week-old mouse femoral head showing the specimen surface at the coronal plane (gray), a representative region of interest (ROI, red cube) for FIB-SEM imaging, the FIB-SEM imaging plane (blue frame, orthogonal to the coronal plane), and the milling direction perpendicular to the imaging plane (red arrow). B) BSE image of a representative tissue section of the femoral head obtained at the coronal plane showing the specimen articular surface (AS), growth plate (GP), calcified cartilage (CC) in the epiphyseal region (left of the growth plate in the image) and metaphyseal region (right of the growth plate). The narrow, irregular cement line (CL, arrow) between bone (B) and metaphyseal calcified cartilage (CC) may be identified by its higher gray value (higher mineral content) on backscattered imaging. The red rectangle, corresponding to the ROI in (A), denotes a representative tissue volume examined more closely with FIB-SEM. The red arrow indicates the milling direction during FIB-SEM. C) Perspective rendering of the three orthogonal planes from FIB-SEM imaging and a reference plane (red/transparent, specimen surface) at the cartilage–bone interface. Fine, dark pores are shown in the blue-framed imaging plane (white arrowheads). These pores correspond to the dark channel structures in the other two orthogonal planes (dark arrowheads). D) A representative energy selective backscattered (EsB) image at the cartilage–bone interface from the volume of the imaging plane of (C) showing calcified cartilage (CC), the cement line (CL, dashed red lines), and metaphyseal bone (B). Aspects of two canaliculi (arrows) appear in the bone region. Numerous, fine, dark pore-like features appear throughout both the calcified cartilage and bone but they are absent from the cement line. E) 3D surface rendering corresponding to (C) and (D) of the extracellular matrix network of calcified cartilage intersecting with a FIB-SEM background image plane and demonstrating numerous nanochannels (cyan) disposed at various angles to the image plane. The many fine, dark pore-like features observed in sections such as that in (D) are transverse profiles of the nanochannels as they intersect the section. The cement line is outlined in red dashes and corresponds to CL shown in (D). As observed in images such as (D) and (E), there is a remarkable size scale difference between canaliculi and nanochannels. A small region of the nanochannel network is enhanced in (F). F) Enlargement of selected nanochannels from the 3D reconstruction presented in (E) with several nanochannels highlighted (dashed frame) for further enlargement in (G). G) Framed region of (F) illustrating multiple branch points (arrowheads) of the nanochannel network.

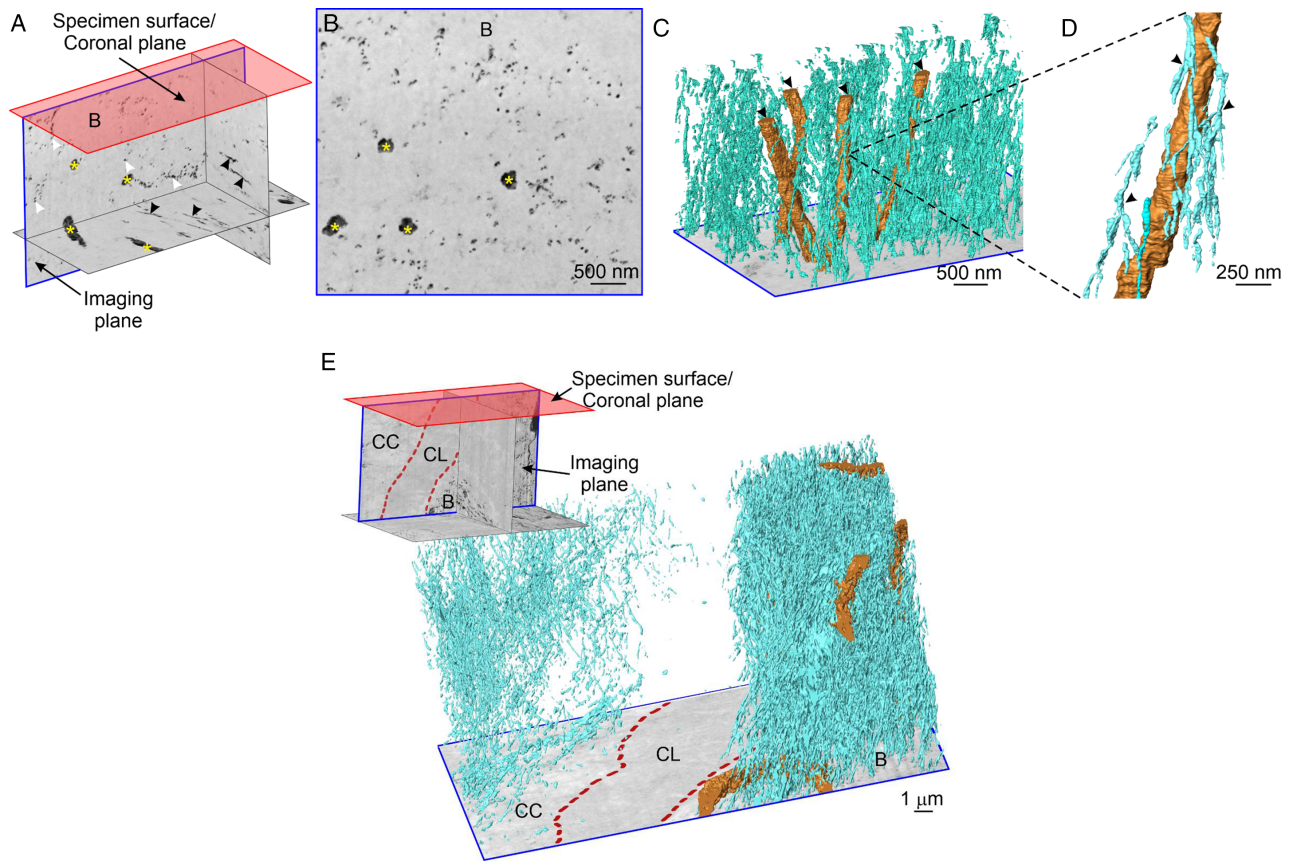


**Figure 3.** FIB-SEM images and 3D reconstructions of the extracellular matrix network at the growth plate calcified cartilage and metaphyseal bone interface of a mouse femoral head. A) Perspective rendering of three orthogonal planes and a reference plane (red/transparent, specimen surface) in the metaphyseal bone region (B) at the cartilage–bone interface. Similar to the structural features detected in cartilage, small, dark pores were found in the imaging plane (white arrowheads). These pores correspond to dark nanochannels in the other two orthogonal planes (black arrowheads). Four bone canaliculi (\*) were also observed in the rendering. B) A representative EsB image from the volume of the imaging plane of (A) showing the bone domain (B) at the cartilage–bone interface of the tissue. Four bone canaliculi (\*) and many associated fine, dark pore-like features are apparent. C) 3D reconstruction corresponding to (A) and (B) and demonstrating the four canaliculi (light brown, marked by arrowheads) and a dense network of nanochannels (cyan) oriented principally in the same direction as that of the canaliculi. The fine, dark pore-like features observed in sections such as that shown in (B) are the transverse profiles of the nanochannels as they intersect the section. A small region of the nanochannel network is enhanced in (D). D) An enlarged image of (C) depicting a single canaliculus (light brown) and its surrounding nanochannels (cyan). Multiple branch points/nodes (arrowheads) of the nanochannels are present, similar to the branching of the nanochannels in calcified cartilage. E) Perspective rendering of three orthogonal planes and a reference plane (red/transparent, specimen surface) of a volume containing calcified cartilage (CC), metaphyseal bone (B), and the cement line (CL) between them (dashed red lines) from a region near the femoral epiphyseal growth plate. The enlarged 3D reconstruction of the volume demonstrates a network of numerous nanochannels (cyan) in both calcified cartilage (CC) and bone (B) that intersect with the FIB-SEM background image plane of the perspective rendering. The nanochannels appear to be denser in the metaphyseal bone compared to the metaphyseal calcified cartilage. There are apparently very few, if any, nanochannels appearing in the cement line (CL, dashed red lines) intervening and separating calcified cartilage from bone. Several osteocyte canaliculi within the bone domain are present (light brown).

within their respective mineralized matrices. Bone had a far higher density (volume percentage) of nanochannels than that of calcified cartilage (4.0% vs 1.7%, respectively, measured from eight volumes examined in each tissue). Nevertheless, in both tissues, the density of nanochannels was much higher than that of bone canaliculi, measured as  $\approx 1\%$  in this study, similar to values reported in the human skeleton.<sup>[20]</sup>

The nanochannels reported here are similar to the size and morphology of a nanochannel system recently discovered by this laboratory in normally mineralizing turkey leg tendon,<sup>[21]</sup> a representative model system for other vertebrate mineralizing

tissues. In turkey tendon, small “secondary channels” ( $\approx 40$  nm in diameter) were found connecting to tenocyte (tendon cell) canaliculi and oriented primarily parallel to the long axes of tendon collagen fibrils. These nanochannels were localized between individual collagen fibrils and maintained a close spatial relationship with presumptive extracellular matrix vesicles, observations suggesting that the nanochannels might play a critical role in passive and/or active transport of mineral ions and/or mineral precursors that lead to collagen mineralization.<sup>[21]</sup> In the current study, no cell processes or matrix vesicles were observed associated with nanochannels in either metaphyseal calcified

cartilage or metaphyseal bone. This result may be attributable to the matrices of both these tissues being fully mineralized in the regions examined and/or to the delicate features and soft tissues (e.g., vesicles, investing membranes) being inadequately preserved or stained.

Given the extent of this newly discovered network penetrating the mineralized matrices of both calcified cartilage and bone, it is possible that the nanochannels represent a fundamental structural framework—a physiological infrastructure—similar to but at a much finer scale than the lacunocanalicular system in bone, which serves to link osteocytes with each other and nearby vasculature.<sup>[11]</sup> Likewise, the nanocanalicular plexus shown here could provide routes for possible ion and molecule transport and exchange between osteocytes in bone, chondrocytes in cartilage, or tenocytes in avian tendon.<sup>[21]</sup> It is known that, particularly for small molecules ( $\approx 400$  Da), transport in cartilage generally occurs by diffusion, driven by the gradients in chemical potential.<sup>[22,23]</sup> It has been proposed that the spaces between the glycosaminoglycan chains on aggrecan molecules (major structural proteoglycans in cartilage) and spaces between collagen fibrils of cartilage ( $\approx 6$  and  $\approx 100$  nm, respectively) provide pathways for molecule transport.<sup>[24]</sup> There are, however, limited experimental data to support such a concept. Further, the lacunocanalicular network in bone has long been regarded as the principal conduit for fluid and solute transport around osteocytes.<sup>[25]</sup> The discovery here of a nanochannel network may lead to new insights into the transport dynamics of ions and molecules in both cartilage and bone. For example, considering the high volume percentage of nanochannels compared to canaliculi, this newly described network might complement or challenge the role of the lacunocanalicular network in osteocyte metabolism and cell–cell signaling. Additionally, the size and the architecture of the nanochannel network documented in this study may provide novel perspectives related to therapeutic molecules that target chondrocytes and osteocytes in osteoarthritis and many other bone, cartilage, tendon, and joint diseases.

Perhaps more striking than the impressive density of the nanochannel network in metaphyseal calcified cartilage and bone is the apparent absence of the network within the cement line, the nanochannels vanishing abruptly at the borders of this region (Figure 2 and 3E, and Movie S2, Supporting Information). This observation suggests the cement line between the two tissues is an impermeable layer, prohibiting direct cartilage–bone interaction and the passage of ion or molecule information. It is well known that the cement line in osteonal bone is rich in osteopontin,<sup>[26]</sup> bone sialoprotein,<sup>[26]</sup> and osteocalcin.<sup>[27]</sup> Osteopontin is a highly charged and phosphorylated noncollagenous protein that has a high affinity to calcium.<sup>[28]</sup> This protein has been suggested to act as an interfacial adhesion promoter (“glue”) between dissimilar tissues, including preexisting and newly formed bone, to maintain the mechanical integrity of biological composites.<sup>[28]</sup> It is intriguing to think that the cement line between metaphyseal calcified cartilage and metaphyseal trabecular bone might also have a high concentration of osteopontin, given that this protein is one of the earliest molecules secreted by preosteoblasts and osteoblasts to their extracellular matrices.<sup>[28]</sup> In this regard, chondrocytes<sup>[29]</sup> and osteoclasts<sup>[30]</sup> are also reported to secrete osteopontin and, together with osteoblasts, it could be conjectured that all three of these cell types may be involved in osteopontin

deposition associated with cement line formation. Indeed, the origin of a cement line is not well understood. Perhaps signals to the cells to remodel the metaphysis lead to osteopontin secretion at a cement line where the protein could conceivably enhance the accumulation of mineral by additional binding of calcium ions and/or coating the surfaces of mineral crystals comprising a newly forming cement line structure. The cement line, in turn, may increase in its mass and density and result in blocking, disrupting, or otherwise preventing the formation or development of nanochannels of both calcified cartilage and bone at the cement line boundary. Studies of any of these suggested possibilities would be useful for elaborating a putative presence and role of osteopontin during cement line deposition as well as development of a cement line itself and its potential effects on nanochannel structure.

### 2.3. Characteristics of Nanochannels and their Association with Mineral Domains in Calcified Cartilage and Metaphyseal Bone

Most vertebrate mineralized skeletal tissues are known to be hierarchically organized and comprised principally of collagen and mineral interacting at multiple size scales.<sup>[31–33]</sup> The demonstration of nanochannels in calcified cartilage and bone in the present work indicates that these tissues also involve, organized and possibly hierarchical nanochannel architectures, which could play distinct roles in tissue physiology. Just as the lacunocanalicular network in bone is thought to influence mineralization, cell–cell communication and healing at the macro- and mesoscale through passage size, density, and branching patterns, for example,<sup>[34,35]</sup> it is conceivable that the architecture of the nanochannel network discovered here offers clues to its formation and function.

To quantify the connectivity of the nanochannels in the calcified cartilage and bone, six metaphyseal calcified cartilage–bone FIB-SEM datasets were chosen from femoral heads of two mice. Following segmentation of nanochannels in each dataset, the network was skeletonized using `scikit-image`<sup>[36]</sup> and its architecture analyzed with an in-house python script based on the `Skann` library.<sup>[37]</sup> Skeletonization resulted in a continuous network representation with channel branches meeting at junctions (“nodes”). Node connectivity was classified according to the number of branches joining each node, with higher numbers of branches indicating higher connectivity.<sup>[38]</sup> For example, 1-N represented a starting or ending point of a nanochannel, while 3-N represented a node with three branches joining it. High node connectivity (e.g.,  $\geq 4$ -N), however, should be interpreted with caution because the skeleton is sensitive to small perturbations of the input shape which could lead to the appearance of spurious branches.<sup>[39]</sup> As shown in **Figure 4**, 3-N and 4-N nodes comprised  $\approx 60\%$  of all nodes in bone, whereas 1-N nodes accounting for  $\approx 20$ – $30\%$ . The remaining nodes ( $\approx 10$ – $20\%$ ) were of higher connectivity ( $\geq 4$ -N). In contrast, calcified cartilage had a higher percentage of branches with one starting/ending point; two of the six datasets in particular showed  $>50\%$  of 1-N and  $<40\%$  of 3-N. Such a difference in the number of nodes between bone and calcified cartilage demonstrated a higher density and greater interconnectivity of nanochannels in the bone matrix compared to that in calcified cartilage. This result is likely related to the fact

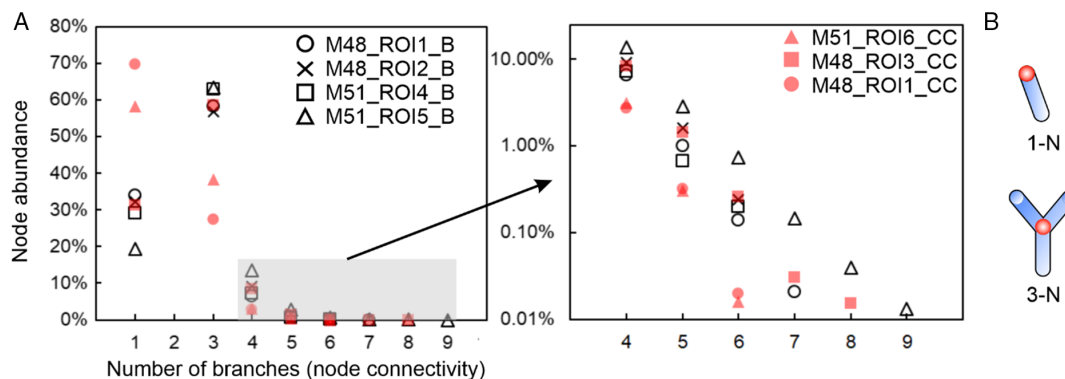


**Figure 4.** Connectivity analysis of the nanochannels in bone (B) and calcified cartilage (CC) after skeletonization of the segmented 3D data. A) Relative abundance of nodes with different numbers of emanating branches in a sampling of ROIs in several skeletonized nanochannel networks found in bone and calcified cartilage from two mouse proximal femoral heads (M48 and M51). The plot to the right with log-scale y-axis shows an enlarged view in the node range from 4-N to 9-N. A total of six FIB-SEM datasets was used for the analysis where one dataset (M48\_ROI1) included both aspects of bone and calcified cartilage. The other five datasets included only bone or calcified cartilage because of the limited field of view. B) Two examples demonstrating the concept of nodes. 1-N represents a starting or ending point of a branch (red sphere). 3-N represents three branches joining a node (red sphere).

that bone has a higher volume percentage of nanochannel networks. The apparent greater density and interconnectivity of passages in bone compared to calcified cartilage may have implications in increased ion or small molecule transport through bone as well as more rapid mineralization and healing in this tissue as opposed to calcified cartilage, but these possibilities require further research to substantiate.

In addition to their branching architectures, nanochannels exhibited a preferred orientation with respect to the cement line plane. The same datasets used for connectivity analysis were further interrogated in terms of the nanochannel orientation in 3D. Branches shorter than 50 nm (a size equal to or less than the diameter of nanochannels) were filtered to increase the accuracy of the 3D presentation of the skeletonized network. For each dataset, a coordinate system was defined with its  $x$ -axis aligned along the milling direction and thus normal to the FIB-SEM imaging plane, its  $y$ -axis aligned normal to the specimen surface/coronal plane, and its  $z$ -axis aligned normal to the  $x$ - $y$  plane and thus parallel to the FIB-SEM imaging plane (Figure 5A). As the cement line plane was roughly parallel to the  $x$ - $y$  plane (yellow-shaded plane, Figure 5A), the  $z$ -axis was pointing approximately normal to the cement line plane (Figure 5A). A spherical coordinate system was specified with theta ( $\theta$ ) as the angle between the endpoint of the branch and the  $z$ -axis (polar angle) and phi ( $\varphi$ ) as the angle between the  $x$ -axis and the orthogonal projection of the branch,  $r$ , onto the  $x$ - $y$  plane (azimuthal angle) (Figure 5A). As shown in Figure 5B,C, the orientation of the nanochannels in the metaphyseal calcified cartilage at the interface showed an interesting correlation with the cement line plane. The nanochannels had a high degree of preferred orientation in which the majority of the nanochannels were almost parallel to the  $x$ - $y$  plane/cement line plane ( $\theta$  about  $80^\circ$ – $90^\circ$ ), and they were aligned roughly along the  $x$ -axis that was perpendicular to the FIB-SEM imaging plane ( $\varphi$  about  $-15^\circ$ ). By pooling the beam length-weighted histograms of  $\theta$  (Figure 5D,E) and  $\varphi$  (Figure 5F,G) from metaphyseal calcified cartilage (Figure 5D,F) and bone (Figure 5E,G), respectively, it was apparent that the nanochannels in both calcified cartilage and bone were

principally parallel to the cement line plane ( $\theta > 80^\circ$ ). However, the nanochannels on the bone side of the cement line interface were more aligned with a narrower distribution of  $\varphi$  values around  $0^\circ$  in all measured samples compared to the more diverse range of  $\varphi$  on the calcified cartilage side of the interface (Figure 5F,G).

There have been no earlier studies concerned with the organization and orientation of nanochannels in any biological tissue except in the mineralizing turkey leg tendon, reported recently by this laboratory.<sup>[21]</sup> In that work, a strong structural correlation was found between the tendon nanochannels and collagen fibrils where the channels were highly aligned with the fibrils. Such a result implies a possible spatial interaction involving these two extracellular matrix constituents, and such a relationship suggesting a putative influence between collagen matrix architecture and nanochannel organization is intriguing to consider in calcified cartilage and bone, for example. In this context of collagen and nanochannels in calcified cartilage and bone, it is interesting to compare results from the present study and two previous small-angle X-Ray scattering investigations of human<sup>[40]</sup> and horse<sup>[41]</sup> cartilage–bone interfaces at the micrometer-scale. The current work reporting nanochannels for the first time did not examine the arrangement of the collagen fibrils at the cartilage–bone interface. The latter two studies, based principally on analyses of the interface beneath articular cartilage in the human and horse, each revealed collagen fibers predominantly parallel to the interface in bone and at a large angle to the interface in cartilage.<sup>[40,41]</sup> The observations of the bone aspect by X-Ray scattering<sup>[40,41]</sup> appear to be consistent with the direction of the highly oriented nanochannels discovered in the metaphyseal bone adjacent to the cement line in the current study. The cartilage aspect examined by X-Ray scattering<sup>[40,41]</sup> is more complicated as the type II collagen fibrils are reported to be randomly distributed without a predominant orientation. This observation makes it impossible to link the fibril arrangement<sup>[40,41]</sup> to the orientation of the nanochannels described in the work here. Further investigation regarding a possible association between the nanochannels in calcified cartilage and bone and their surrounding

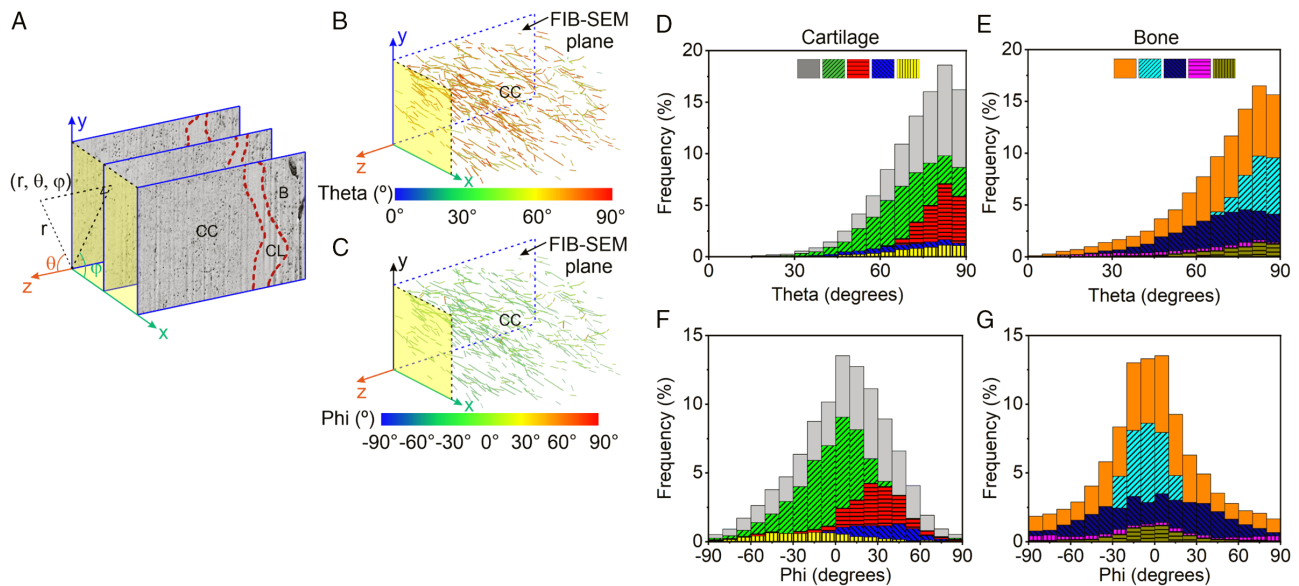


**Figure 5.** Orientation of nanochannels in the metaphyseal calcified cartilage and metaphyseal bone at the interface of a mouse femoral head. A) The spherical coordinate system with respect to a stack of FIB-SEM images showing the cement line (CL, dashed red zone) located between calcified cartilage (CC) and bone (B). The  $x$ -axis of the coordinate system is defined perpendicular to the FIB-SEM images and parallel to the milling direction. The  $y$ -axis is perpendicular to the specimen surface and the  $z$ -axis is pointing in the direction roughly perpendicular to the cement line plane. Rho ( $r$ ), the radial distance, is shown as the line connecting the origin of the coordinate system and the measured object. Theta ( $\theta$ ), the azimuthal angle, is given as the angle between  $r$  and the coordinate  $z$ -axis. Phi ( $\varphi$ ), the polar angle, is defined as the angle between the projection of  $r$  onto the  $x$ - $y$  plane (yellow-shaded area) and the coordinate  $x$ -axis. B) A representative 3D depiction of skeletonized nanochannels in metaphyseal calcified cartilage (CC) depicted as color-coded theta ( $\theta$ ) in the above defined coordinate system. The majority of the nanochannels are coded as orange/red, corresponding to  $\theta$  of approximately  $80^\circ$ – $90^\circ$ . The yellow-shaded plane in (B) corresponds spatially to the yellow-shaded plane in (A). C) The same 3D tissue volume as shown in (B) and illustrating nanochannels in metaphyseal calcified cartilage (CC) color-coded with phi ( $\varphi$ ) values. The skeletonized nanochannels are principally light green, corresponding to  $\varphi$  of approximately  $-15^\circ$ . D,E) Beam length-weighted histograms of  $\theta$  of nanochannels measured from four different ROIs in each of metaphyseal cartilage (D) and metaphyseal bone (E). The majority of  $\theta$  is centered about  $80^\circ$ – $90^\circ$ . F,G) Beam length-weighted histograms of  $\varphi$  of nanochannels measured from the same four ROIs as in (D) and (E).  $\varphi$  has a varied distribution in metaphyseal cartilage (F) while  $\varphi$  tends to center about  $0^\circ$  in metaphyseal bone (G). Gray bar plots in (D and F) and orange bar plots in (E and G) represent the summed histogram from all measured ROIs in the respective cartilage or bone domain. The four other colors and patterns of the bar plots of (D and F) and (E and G) denote different ROIs in the respective calcified cartilage and bone domain.

collagenous matrix might provide more insight into the factors governing nanochannel formation and its possible involvement with ECM architecture.

While there was an organized alignment of the nanochannels in both metaphyseal cartilage and bone, they were not distributed homogeneously throughout these tissues. In 2D slices, nanochannels instead often appeared to form a periphery around “domains” of highly mineralized structures. **Figure 6A** shows several domains in metaphyseal calcified cartilage, adjacent to the cement line. Through successive slices in FIB-SEM image stacks (Figure 6B), mineral domains changed in size and shape, associated with varying numbers and locations of small, dark, punctate features, representing peripheral nanochannels. Manual segmentation and 3D reconstruction revealed the domains to be closely packed and to have a tapered pillar or columnar morphology, elongated along the axis perpendicular to the imaging plane (Figure 6C,D). Reconstructed domains were  $\approx 1$ – $1.5 \mu\text{m}$  in diameter and  $\approx 1.5$ – $2.5 \mu\text{m}$  long and were closely related structurally to the nanochannels describing their contours (Figure 6D). It should be noted, however, that the seeming elongation of such domains could also be attributed to the agglomeration of two or more smaller domains along their long

axis. Given that regions closer to the mineralization front might provide insight into the possible correlation between nanochannels and mineral domains, lower resolution FIB-SEM images with larger fields of view were taken close to the nonmineralized growth plate cartilage (red-dashed rectangle; Figure 6E). With distance from the growth plate, the boundaries between domains gradually became obscure, and it was impossible to identify clear domain boundaries next to the highly mineralized cement line at the cartilage–bone interface (Figure 6E). While domain boundaries were increasingly more difficult to define, the nanochannels described above appeared more obvious (Figure 6A,B). 3D surface rendering of selected mineral domains near the growth plate (red-dashed rectangle; Figure 6E and F) and the cement line (Figure 6C,D) showed them as irregularly spherical or ellipsoidal in shape. Interestingly, FIB-SEM data acquired from a similar anatomical region, but a demineralized specimen stained with osmium-thiocarbohydrazide to enhance soft tissue contrast,<sup>[42]</sup> showed domains of similar shape and size to those observed in mineralized specimens (Figure 6G, yellow-dashed circles). These domains also resembled the “crystal ghosts” described previously by Bonucci in demineralized cartilaginous tissues.<sup>[43–45]</sup> The brighter contrasting components of the



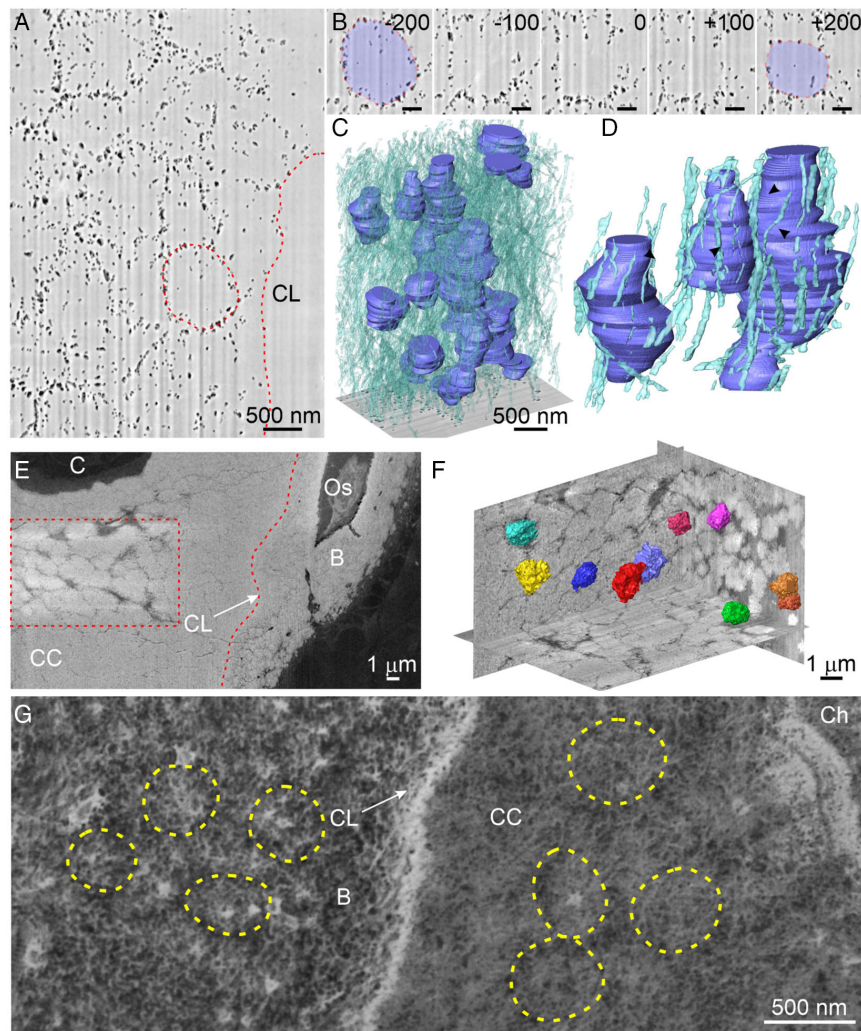


**Figure 6.** Mineralization domains in the metaphyseal calcified cartilage region of a mouse femoral head. A) A high-resolution secondary electron (SE) image of calcified cartilage at the cartilage–bone interface near the cement line (CL, dashed red line defining one of its two surfaces) showing many abutting mineral domains apparently surrounded and bounded by fine dark features. One such domain is marked by a dashed red ellipse. Such domains are visually approximated and may capture some fine, dark features within them. B) A sequence of five FIB-SEM images showing the mineral domain identified in (A) (dashed red ellipse, light purple) within calcified cartilage of the tissue. Numbers at the top right corners of the panels represent the distance (nm) of each image from the reference image (marked by 0) along the imaging direction (approximately along the inferior–superior axis of the femoral head) in the specimen volume investigated. The mineral domain, defined by surrounding small, dark, punctate features, changes in size and shape with distance along the imaging direction. Scale bars = 250 nm. C) 3D reconstruction corresponding to a portion of (B) including the domain enclosed by the dashed red ellipse along with additional neighboring mineral domains and the fine, dark punctate features as observed in (A,B). The reconstruction shows the domains (purple) are pillar- or columnar-shaped of somewhat irregular diameter and shape and oriented in approximately the same direction, perpendicular to the image plane. Nanochannels (cyan) surround the pillars and appear to define pillar shape. D) 3D rendering of three mineral pillars (purple) and their associated nanochannels (cyan) showing that the nanochannels closely follow the contours of the domains (arrowheads). The disc-like shapes comprising the cartilage mineral pillars result from segmentation and reconstruction and are artifactual structures. Pillars represent bundles of mineralized type II collagen fibrils in the calcified cartilage of the growth plate of the mouse femoral head. E) Low-resolution EsB image overview at the cartilage–bone interface showing calcified cartilage (CC) and bone (B), the cement line (dashed red line, CL) and aspects of a chondrocyte (Ch) and an osteocyte (Os) residing in their lacuna. This image shows rounded or elliptical-shaped domains of calcified cartilage defined by darker features bounding them (box enclosed by dashed red lines). F) Perspective rendering of three orthogonal planes and 3D surface rendering of a few selected mineral domains from the enclosed box region in (E) illustrates mineral domains of calcified cartilage in irregular spherical or ellipsoidal shapes. G) A representative FIB-SEM image of a demineralized mouse femoral head sample stained with osmium-thiocarbohydrazide and showing bone (B), the cement line (CL), calcified cartilage (CC), and part of a chondrocyte (Ch). Several domain-like patterns of matrix (dashed yellow circles) are apparent in the decalcified cartilage and bone aspects of the image.

domains were proposed to contain acidic proteins that bind and stabilize amorphous calcium phosphate at the outset of mineralization and eventually lead to the formation of crystalline hydroxyapatite.<sup>[44,45]</sup>

Based on the appearance of the mineral domains as noted above—their size and shape, organization, orientation, and spatial relation with neighboring domains—and their co-occurrence with nanochannels but not with cells, a new model is proposed here by which mineralized tissue growth can progress independently of cellular control and the nanostructural features that are demonstrated in this study form as a consequence of this growth mechanism. The proposed process is analogous to one in traditional materials engineering, where loose fine particles in suspension are sintered into a solid coherent mass through diffusion at the boundary of particles, causing necks to form and grow at these contact points.<sup>[17]</sup> As the particles increase in size and the distance between them decreases, capillary action pulls the liquid into the smaller interstitial recesses between particles. In areas where capillary pressures are high, atoms will preferentially enter into solution and precipitate, and smaller particles will redeposit on nearby surfaces of larger particles or in areas where particles are not in close contact and have lower chemical potential. The resultant phenomenon is a hierarchical assembly and compaction process known as Ostwald ripening.<sup>[46]</sup> In the mineralized skeletal tissues examined here, considering the small size of the nanochannels ( $\approx 10\text{--}50\text{ nm}$ ), it is plausible that they create high capillary forces that facilitate the transport of mineral ions and/or precursors. Such ions or precursors could then aggregate and nucleate at various locations both within and outside collagen fibrils. In this way, the columnar mineral domains observed in this study could develop without biological control, purely through a physicochemical process without a source of external energy input (heat or pressure, for instance) as in traditional materials engineering, whereby mineral foci grow into abutment through passive sorting and distribution of ions/particles in the interstices between growing mineral clusters (Figure 7). In this model, the nanochannels

observed here would form during tissue maturation as the remnants of peripheral spaces between maturing mineral domains (Figure 7), and they would comprise a distribution network and be the by-product of the proposed “biological sintering” process.

The presence of nanochannel and mineral domain patterns in both calcified cartilage and bone—tissues based on different collagen types and with different meso- and macroscale architectures—argues that the proposed assembly process could be a fundamental and shared mechanism for the construction of mineralized skeletal tissues at the nanoscale. Indeed, recent FIB-SEM studies in mineralizing turkey leg tendon<sup>[21]</sup> and mouse<sup>[14]</sup> and human lamellar cortical bone<sup>[15]</sup> revealed similar prolate ellipsoidal microsized mineral clusters, which were suggested to develop from nanoscale spherulitic mineral foci growing along and across the matrix collagen fibrils of these tissues. Nanochannels were also found to occupy the spaces between collagen fibrils in the turkey leg tendon.<sup>[21]</sup> These several studies,<sup>[14,15,21]</sup> however, principally focused on mineralization fronts or regions at early stages of mineralization where individual mineral ellipsoids could be clearly visualized, as in the samples close to the growth plate in the present report (Figure 6E,F). The current work gives perspective to those previous results by providing a detailed depiction of the meso- and nanostructure of calcified cartilage and bone at later stages of mineralization, giving developmental and mechanistic context to these tissue morphologies.

#### 2.4. Chemical Composition of the Nanochannel Contents and Their Indication for the Mineralization Process

The nanochannel network that is described here offers the potential for extensive (and previously unappreciated) access to calcified cartilage and bone tissue deep within the femoral head. The contents of the nanochannels can provide clues as to whether these minute passages are more actively involved in building tissues or structural by-products of a growth process as detailed in Section 2.3. Characterizing the contents of nanochannels,

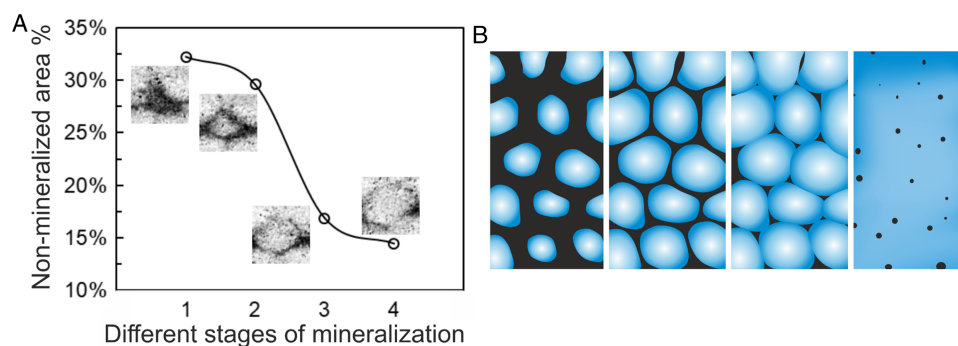


**Figure 7.** A) A series of FIB-SEM images from the same stack with corresponding quantification of the area fraction of nonmineralized tissue and B) schematic illustration showing the proposed development of mineralization in calcified cartilage and bone. (A) The four FIB-SEM images represent mineralization occurring at different degrees at the specific location imaged. The distance between two successive images is  $\approx 170\text{ nm}$ . As the degree of mineralization increases (stages 1–4), the area fraction of nonmineralized tissue decreases. The area fraction of nonmineralized tissue in each FIB-SEM image was acquired by using a set threshold. (B) Correlated with the stages depicting the observed increase in mineralization, left-to-right panels show conceptually the increase in size of a group of neighboring mineral domains (blue) in solution and their coalescence with each other. Increasing mineral domain size comes at the expense of solution volume (black), which decreases. Eventually the individual domains form a solid coherent mineralized tissue with small solution porosities (far right panel, small dark circles). The process resembles sintering of traditional materials, such as liquid phase sintering of alloys and composites.<sup>[16]</sup>

however, is methodologically challenging, requiring careful physical isolation of very small volumes to ensure that materials internal and external to nanochannels are not conflated in analysis. To approach this issue of understanding the ultrastructural and compositional nature of the nanochannel contents more completely, FIB was used to isolate regions across the metaphyseal calcified cartilage and bone interface and prepare thin sections of the tissues for transmission electron microscopy (TEM) investigations. Two lamella samples ( $\approx 100\text{--}200\text{ nm}$  thick) were successfully prepared from two mouse femoral heads. Observed under bright-field TEM, these ultrathin samples contained numerous nanochannels which appeared in calcified cartilage and bone (Figure 8A) to be disorganized and disposed in various directions

in their through-thickness projections. However, a few nanochannels were found oriented perpendicular to the image plane, visible as electron transparent voids (Figure 8a,b; arrowheads). This perspective with unobstructed views down a short and relatively straight section of a nanochannel provided relatively unadulterated regions of consistent composition, where a structure visible on the surface (a nanochannel wall or lumen, for example) could be presumed to continue in the Z-direction. This sample preparation therefore permitted fine scale, region-specific imaging by TEM and compositional characterization by EDX of mineralized and nonmineralized tissues associated with the nanochannels, as well as selected-area electron diffraction (SAED) measurement approaches that average through sample thickness.

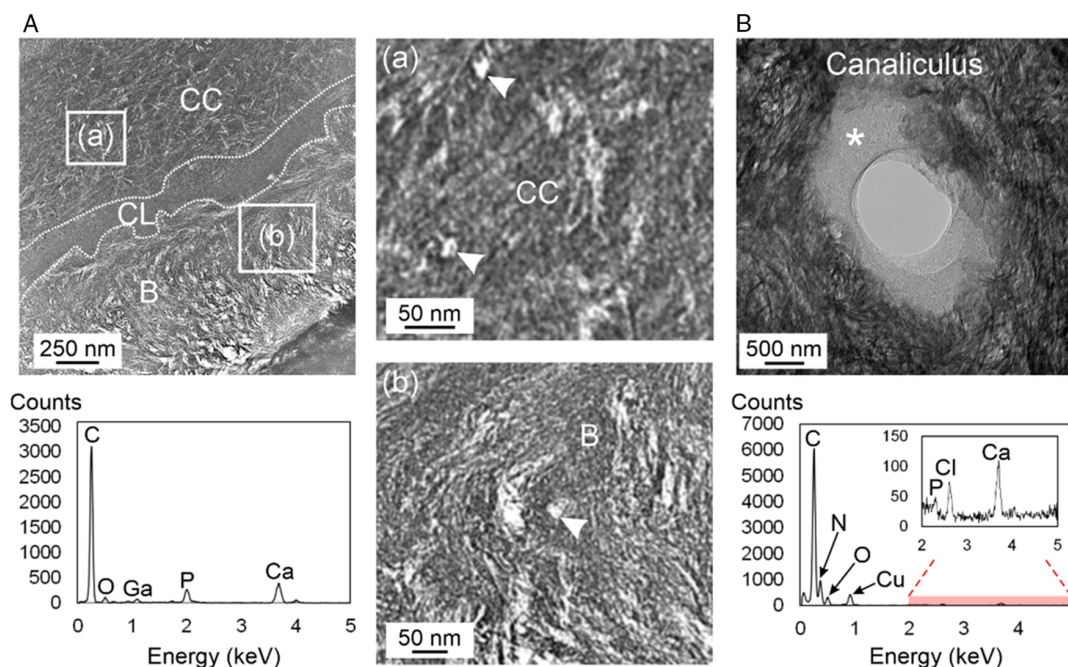


**Figure 8.** TEM and corresponding EDX spectral analysis of  $\approx 100\text{nm}$ -thick tissue slices at the cartilage–bone interface of the mouse femoral head. Representative TEM micrographs are illustrated together with an example below the image of an EDX spectrum obtained from tissue sites represented by the corresponding TEM images. A) Micrographs show metaphyseal calcified cartilage interfacing bone at the cement line and an enlargement of nanochannels in calcified cartilage (a) and bone (b), B) a canaliculus in metaphyseal bone, C) metaphyseal trabecular bone matrix, D) metaphyseal calcified cartilage matrix, and E) an interface between metaphyseal calcified (black) and noncalcified (gray) cartilage matrices. (A) Bright-field TEM image at the cartilage–bone interface revealing different structures in the metaphyseal calcified cartilage (CC), cement line (CL), and metaphyseal bone (B) of the specimen. Two regions, (a) from calcified cartilage and (b) from bone, have been enlarged to show electron-transparent voids/nanochannels visible in these tissue aspects with some nanochannels oriented perpendicular to the image plane (a and b, arrowheads). There were no observable voids/nanochannels or any recognizable structural features in the cement line. EDX spectra were obtained from nanochannels in transverse profile, similar to the ones shown in a and b. (B) A single canaliculus in transverse profile in bone showing a central hole surrounded by organic material (gray) and mineralized bone tissue (black). The portion of the organic matrix examined by EDX is marked (asterisk) and the corresponding spectrum is shown below the TEM image. Higher energy aspects (2–5 keV) of the spectrum were expanded in the inset to show some elements more clearly. (C) A representative area of a fully mineralized metaphyseal trabecular bone region near the cement line. The EDX spectrum presented below the TEM image was obtained from an area similar to that shown in the TEM image. (D) A region of metaphyseal calcified cartilage near the cement line showing numerous nanochannels penetrating the matrix (arrowheads). The electron dense/mineralized area was used to generate the corresponding EDX spectrum. (E) The interface between noncalcified growth plate cartilage (gray) and calcified cartilage (black). The noncalcified cartilage matrix was analyzed with EDX. Carbon, a background element, was detected in all EDX spectra and was notably higher in nanochannels (A), canaliculi (B), and noncalcified cartilage (E). Nanochannels (A) and canaliculi (B) were found to contain limited amounts of phosphorus and calcium and traces of nitrogen and oxygen. Bone (C) and calcified cartilage (D) appeared enriched in calcium and phosphorus with a notable amount of oxygen. Noncalcified cartilage matrix (E) was predominantly comprised of carbon with traces of nitrogen and oxygen. Traces of chloride and magnesium were also found in canaliculi (B) and bone matrix (C), respectively. Ga from the FIB beam source was detected because of the lamella preparation process for bone (C) and calcified cartilage (D). Cu in all spectra originated from the TEM grid as a background element. The calculated range of the atomic weight percentage of each major element detected in the different types of tissues together with the number of ROIs measured over five sections is summarized in the table below the EDX spectra.

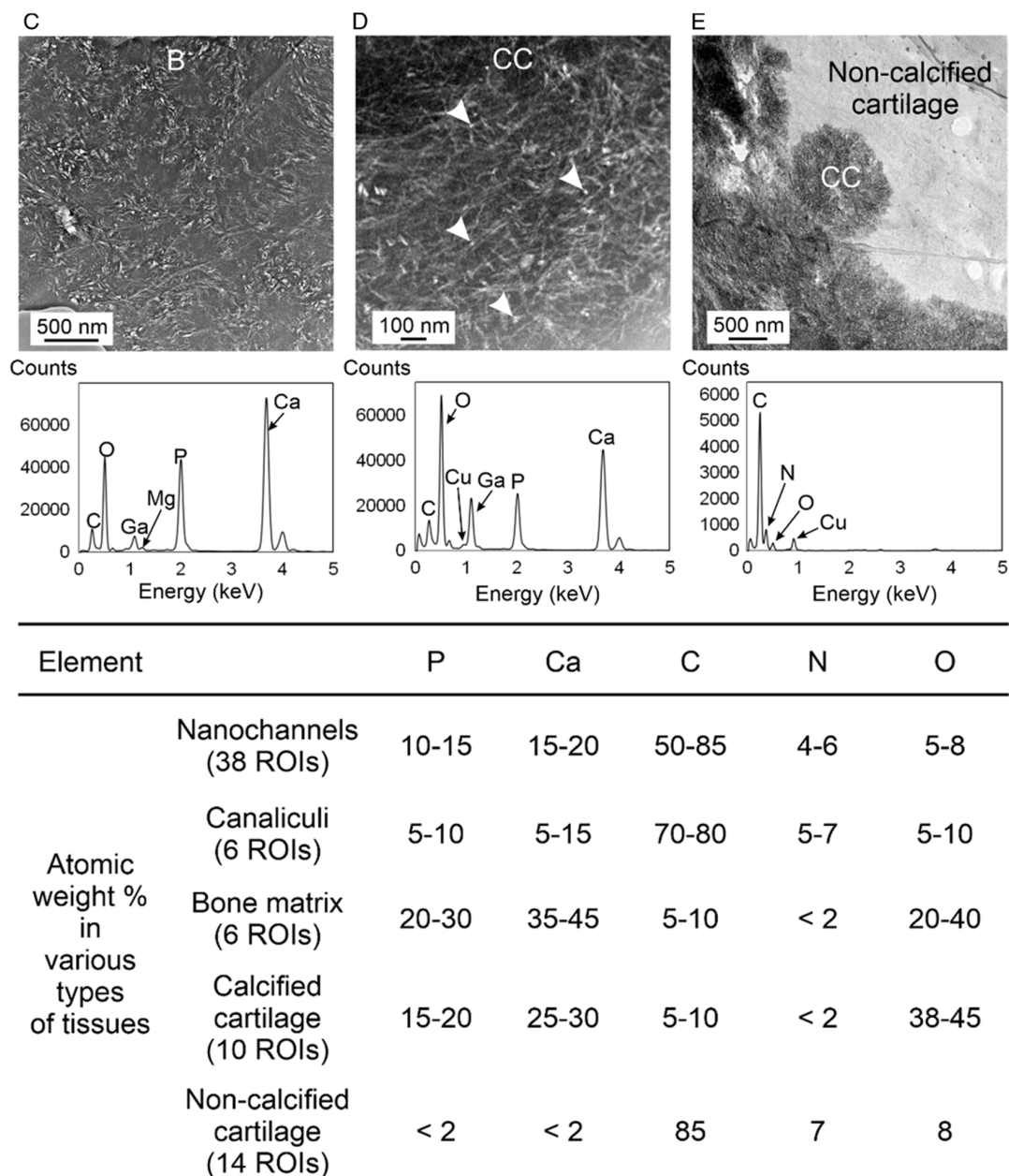


**Figure 8.** Continued.

Within the bone aspect, “lacy” domains (pinwheel motifs of curved mineral particles a few nm wide) were observed in the tissue surrounding both the nanochannels and canaliculi (Figure 8A and S3A, Supporting Information). Such domains were similar in morphology to lacy motifs reported in previous bone studies.<sup>[47,48]</sup> Notably in contrast to the calcified cartilage and bone, no discernable nanochannels could be recognized in the cement line itself, where mineral crystals having sizes of  $\approx 5\text{--}10$  nm were embedded within an organic matrix (Figure 8A and S3C, Supporting Information). This observation supported the present FIB-SEM results, suggesting the cement line was most likely a physical barrier between calcified cartilage and bone.

Insight into the mineral component of the tissues was obtained utilizing diffraction techniques as noted above. SAED patterns obtained from calcified cartilage, bone, and the intervening cement line are shown in Figure S3 (Supporting Information). Despite a limited number of diffracting crystals in the analyzed volumes of the cement line (Figure S3C, Supporting Information) compared to the number of such crystals in metaphyseal bone (Figure S3A, Supporting Information) and metaphyseal calcified cartilage (Figure S3B, Supporting Information), all diffraction patterns were indicative of polycrystalline hydroxyapatite with clear diffraction reflections related to the (002) and (211) planes of the mineral (Figure S3, Supporting Information).

EDX analysis of the chemical composition of several aspects of the mouse femoral head yielded certain interesting results. Carbon was detected in all samples examined and its presence may derive from the organic matrices of the femoral head tissues, the PMMA embedment for the samples, or as a general spectroscopic contaminant. As expected for these mineralized tissues, metaphyseal bone (Figure 8C) and calcified cartilage (Figure 8D) generated prominent signals of calcium, phosphorus, and oxygen together with traces of magnesium, the latter being a common substitute in apatite for calcium. Oxygen may originate from apatite or the PMMA. Other tissue regions with mineral that were examined, the calcified cartilage and bone with nanochannels (Figure 8a,b, respectively) and the bone canaliculi (Figure 8B), also produced calcium, phosphorus, and oxygen signals as well as nitrogen, likely from the organic protein content of these samples. Spectra from noncalcified growth plate cartilage (Figure 8E) showed nitrogen and oxygen, again likely from protein (nitrogen) and PMMA (oxygen). The aspect of the bone canaliculus around its central hole provided signals of calcium, phosphorus, oxygen, and nitrogen (Figure 8B) and the same elements were found on EDX analysis of nanochannels in the samples (Figure 8A). These elements may derive, in part, from the mineral surrounding the canaliculus and from the organic protein matrix (nitrogen) of this sample area. In this regard, such local compositional measurements could incorporate some sampling as a result of secondary scattering from nanochannel walls and other structures adjacent to the sites directly excited by electron beam, given the sizes of these passages and the cone-shape of the electron beam. However, the controlled sample preparation utilized in the present study, the differing elemental proportions with surrounding tissues, and the suggestion of phosphorus in both nanochannels and canaliculi support a more exciting possibility with particular relevance for tissue physiology.

With regard to the canaliculi (Figure 8B) and nanochannels (Figure 8a,b) in the samples, their carbon and nitrogen content indicates the presence of organic molecules, possibly attributable to the PMMA embedment or protein components such as collagen, as noted above. Calcium, phosphorus, and oxygen may originate from apatite, mentioned previously, as a result of secondary scattering nearby the sites directly excited by electron beam impingement during EDX. Another source of phosphorus from a speculative viewpoint may be free orthophosphate ( $\text{PO}_4^{3-}$ ) and/or phosphorylated compounds putatively comprising the organic matrix aspects of canaliculi and nanochannels. In this context, numerous phosphorylated species have been implicated in the inhibition of mineralization in skeletal tissues. Perhaps such phosphorylated molecules serve as inhibitors to mineral deposition because canaliculi and nanochannels remain unmineralized to maintain the patency of fluid space in the otherwise fully mineralized bone and calcified cartilage tissue matrices. Indeed, it is known that bone osteocytes synthesize and secrete several noncollagenous, phosphorylated bone matrix proteins, including osteopontin and dentin matrix proteins, which have a high capacity to bind calcium and inhibit mineralization.<sup>[49]</sup>

Other phosphorylated mineralization inhibitors occurring in mineralizing vertebrate tissues include pyrophosphate and polyphosphate, which are present in the circulation of vertebrates.

Pyrophosphate, the smallest member of the polyphosphate family, prevents mineral formation and growth and serves as an extremely potent inhibitor for tissue mineralization.<sup>[50]</sup> Polyphosphate, having multiple negatively charged phosphate groups promoting ionic interactions with calcium, can also act as an inhibitor in the mineralization process.<sup>[51]</sup> Both pyrophosphate and polyphosphate thus permit storage of high concentrations of bioavailable orthophosphate without forming mineral crystals in the circulation. Possibly, EDX phosphorus signals are attributable to pyrophosphate and polyphosphate molecules that have been fixed and localized within the canaliculi and nanochannels reported in this study. In any case, whatever the source of phosphorus during EDX analysis and whether phosphorylated molecular species contribute to the structure of canaliculi and nanochannels, the latter may provide the space and fluid environment to allow the transport of various ions and small molecules to mineralization sites within and throughout the extracellular matrices of calcified cartilage and bone.

Similarly, proteoglycans, though not phosphorylated, can also inhibit mineralization by virtue of their numerous sulfate groups that may bind calcium.<sup>[52–54]</sup> Proteoglycan content can therefore also be an indicator of local mineralization inhibition. For example, perlecan, a type of proteoglycan, has been shown to contribute to maintaining open lacunocanalicular channels as mice lacking this molecule were found to exhibit unusually narrow canaliculi.<sup>[55]</sup> To test whether nanochannels observed in the present work contained proteoglycans or increased levels of these molecules, a mouse femoral head was demineralized and stained with Alcian blue followed by osmium-thiocarbohydrazide.<sup>[56]</sup> Initial histological results showed that the demineralized cartilage of the femoral head was generally more highly stained compared to the demineralized bone (Figure 6G), a result suggesting a higher proteoglycan content and greater inhibition potential for mineralization in cartilage compared to bone.

More work is necessary to verify whether the organic matrices of calcified cartilage and bone nanochannels are indeed rich in mineralization inhibitors (proteoglycans, phosphorylated compounds). However, the findings here indicate that such inhibitors could provide a means to facilitate the maintenance of fluid space within completely mineralized bone and calcified cartilage matrices, offering persistent access for various ions and small molecules to permeate surrounding extracellular matrices and reach even their most remote sites destined to mineralize.

## 2.5. Potential Limitations of This Study

The question of artifacts is often raised in a discussion of the detection and characterization of structural components of a tissue by microscopic means, particularly high-resolution approaches such as FIB-SEM. In the current work, it is conceivable that FIB-SEM could inadvertently lead to artifacts resulting from either sample preparation or the imaging technique itself. However, the nanochannel morphologies presented in this study are comparable to those obtained in an earlier investigation of turkey leg tendon, in which tissue was prepared by traditional chemical fixation as well as high-pressure freezing and freeze substitution and then examined by both TEM and

FIB-SEM.<sup>[21]</sup> The similarities between the tendon dataset and the present results suggest that nanochannels are not induced by the methodologies applied in this current FIB-SEM study. In addition, similar ellipsoidal mineral domains/clusters observed in the present investigation using FIB-SEM have been reported by other groups.<sup>[14,15]</sup> The TEM sections prepared by FIB lift-out from the area adjacent to that subjected to 3D FIB-SEM imaging in the present work showed the classic “lacy” patterns of bone. Such “lacy” patterns have been repeatedly documented in other studies (e.g., by Reznikov et al.<sup>[47]</sup>), where tissues were prepared by a variety of techniques, including conventional, anhydrous, and cryofixation methods. The presence of these tissue features (ellipsoidal mineral domains/clusters and “lacy” bone), observed by different types of microscopy techniques after a variety of sample preparative methods, further diminishes concerns that they are artifactual.

### 3. Conclusions

FIB-SEM 3D imaging at the interface of metaphyseal calcified cartilage and metaphyseal trabecular bone has revealed a complex and extensive extracellular matrix network comprised of well-known osteocyte canaliculi in the bone tissue<sup>[11,35,57]</sup> and now additionally a network of nanochannels in both the calcified cartilage and bone. The absence of nanochannels in the cement line supports their being biological, nonartifactual structural features, while connoting that the cement line could act as a physical barrier, isolating calcified cartilage and bone fluid compartments. The nanochannels have higher connectivity within the bone aspect and were oriented principally parallel to the plane of the cement line, which itself lacks any nanochannels. The nanochannels were found to have a close association with individual domains of mineral having a tapered, “pillar-like” structure. These morphologies are suggestive of nanochannels having formed as a result of a mineralization process analogous to the reduction of liquid space between particles during sintering in traditional powder metallurgy and ceramics processing. High carbon and phosphorus elemental composition of the nanochannels contends that these passageways might serve as reservoirs for phosphorylated molecules inhibiting mineralization in addition to their facilitating transport of ions and small molecules for the growth and aggregation of tissue mineral domains.

The presence of nanochannels remains to be verified in other anatomical sites (the mouse proximal/distal tibia, for example) and other mammalian taxa (such as humans), and definitive identification of the organic content of nanochannels through immunocytochemical techniques, for instance, will be vital for determining their importance and physiological role. However, the study herein advances current knowledge and understanding of the ultrastructure of the cartilage–bone interface not previously appreciated in the literature. Moreover, the demonstration of a nanoscale network that is pervasive and nearly ubiquitous in mouse femoral tissues opens the possibility that an overlooked and clinically relevant transport medium exists for providing widespread and deep access into the mineralized tissues of the vertebrate skeleton.

### 4. Experimental Section

**Nondemineralized Specimens:** Six 9 week-old, female BALB/c mice were examined in total. The work was approved by the Institutional Animal Care and Use Committee (IACUC) of Cornell University (Ithaca, NY, USA) where the animals were maintained and subsequently sacrificed. Immediately following harvest, proximal femora of the mice were carefully cleaned with a scalpel of attached muscles, tendons, and ligaments. The femora were then fixed in 4% paraformaldehyde (Electron Microscopy Sciences, Hatfield, PA, USA) in phosphate-buffered saline solution (PBS; Sigma-Aldrich, St. Louis, MO, USA) for 16 h, followed by rinsing in 0.01 M PBS (Sigma-Aldrich) for 48 h. The femora were next dehydrated in a graded ethanol series (70%, 80%, 96%, 100%; 2 days for each step at 4 °C), stained with 0.004% w/v rhodamine 6G (Thermo Fisher, Waltham, MA, USA) in ethanol for 1.5 days twice at 4 °C, and defatted in xylene for 3 h twice at 4 °C before embedding in the low-temperature embedding system, Technovit 9100 New (Heraeus Kulzer GmbH, Hanau, Germany).<sup>[58]</sup> All embedded femora were cut with a low-speed diamond wire saw (150–250 µm diameter; Diamond WireTec GmbH&Co.KG, Weinheim, Germany) at the coronal plane to expose the cartilage–bone interface below the growth plate (Figure 1A–C). The coronal sections obtained were subsequently ground with a series of carbide grinding papers and polished with diamond suspensions to improve surface smoothness for experiments.

**Demineralized and Proteoglycan-Stained Specimens:** Two freshly frozen mouse femoral heads (C57/BL6, female, 10 week-old) and two knee joints (cut at the sagittal plane) were demineralized using a solution of 5% ethylenediaminetetraacetic acid (EDTA, Avantor, PA, USA) and 4% paraformaldehyde (PFA, Electron Microscopy Sciences) in 0.2 M cacodylate buffer (Electron Microscopy Sciences) at pH 7.4. The C57/BL6 mouse strain has a similar ossification pattern at the femoral head compared to that of the BALB/c mouse strain.<sup>[18]</sup> Upon demineralization, the specimens were washed four times (each time about 8 h) using a 0.1 M cacodylate buffer (Electron Microscopy Sciences) to remove residual EDTA. Afterward, the specimens were fixed with 4% glutaraldehyde in 0.2 M cacodylate buffer at pH 7.4 overnight at room temperature followed by washing with cacodylate buffer four times. To assess the presence of mucosubstances (proteoglycans and glycoproteins), the two femoral heads and two partial (half) knees were stained overnight with 0.6% Alcian blue (Sigma-Aldrich) and then washed with cacodylate buffer (0.2 M) three times (the other two partial knees were not stained with Alcian blue and used as control tissues). Alcian blue is a cationic dye that binds to polyanions and, in conjunction with glutaraldehyde, it preserves mucosubstances.<sup>[59]</sup> Finally, all specimens were stained by the sequential applications of osmium tetroxide (Electron Microscopy Sciences) and thiocarbohydrazide (Sigma-Aldrich) as reported by Reznikov et al.<sup>[42]</sup> The specimens as described above were subsequently embedded in EPON resin (Electron Microscopy Sciences) following the protocol given by Maria et al.<sup>[60]</sup> All the embedded specimens were ground and polished with the same procedure as mentioned above for the nondemineralized specimens.

**Micro-CT:** A micro-CT imager (RX Solutions EasyTom160/150 tomographic unit, Chavanoz, France) was used to scan the nondemineralized mouse femora before the embedding procedure described above. While immersed in 70% ethanol, the entire femurs and their femoral heads were imaged at a resolution of  $\approx 8.5$  and  $\approx 1.5$  µm per voxel size, respectively. X-Act CT software (RX Solutions) was utilized to reconstruct the projection images.

**SEM:** All prepared specimens were imaged with a Quanta 600 FEG environmental scanning electron microscope (FEI, Hillsboro, OR, USA) using a BSE detector in low vacuum mode. Samples were uncoated and imaged at 0.75 Torr with 12.5 kV beam voltage.

**Histology:** For each nondemineralized sample, serial sections of 8 µm were cut using a Leica microtome (Leica Biosystems Nussloch GmbH, Nussloch, Germany) and stained with 0.5% Alcian blue combined with 0.1% Picrosirius red. Successive sections were stained with Goldner's trichrome. All stained specimens were examined under bright-field using a white light optical microscope (Leica DM RXA2 and DM RA2; Leica

Microsystems and Zeiss AxioLab 5, Carl Zeiss Microscopy, Konstanz, Germany) equipped with 20×, 40×, and 50× objective lenses.

**FIB-SEM:** For nondemineralized specimens, an iodine vapor method was employed to increase the differential contrast of soft tissue and cell components.<sup>[61]</sup> FIB-SEM in serial surface imaging mode was performed with a Zeiss crossbeam 540 station (Carl Zeiss Microscopy) to examine both nondemineralized and demineralized specimens. Carbon-coated specimens were oriented inside the FIB-SEM chamber so that the viewing direction was aligned approximately parallel to the growth plate and the cement line between calcified cartilage and bone of the mouse femoral heads. Such orientation allowed FIB-SEM images to be taken across and perpendicular to the cement line (Figure 2A). A coarse rectangular section was first milled with a 30 or 65 nA Ga ion beam at 30 kV acceleration voltage to provide a viewing channel for SEM observation. The exposed surface of the rectangular section was fine-polished by lowering the ion beam current to 1.5 or 3 nA. Subsequently, the fine-polished block was serial-milled by scanning the ion beam parallel to the surface of the cutting plane using an ion beam of 100, 300, or 700 pA at 30 kV. After removal of each tissue slice, the freshly exposed surface was imaged at 1.6–1.8 kV acceleration voltage and 600 or 700 pA using both SE and EsB detectors. The slice thickness was roughly equivalent to the lateral resolution of 2D images, ranging from 2.5 to 12.9 nm. In a fully automated procedure, the milling was combined with SEM imaging in sequence (imaging, then sectioning and reimaging) to collect thousands of serial images. Serial images were aligned (image registration) with an in-house python script in Anaconda (Anaconda Inc., Austin, TX, USA) followed by reduction of curtaining effects and removal of background noise. The resulting stacks of images were then segmented according to their structural features and reconstructed using Amira-Avizo (v 2020.1; Thermo Fisher Scientific and Zuse Institute, Berlin, Germany) and Dragonfly (v 4.1; Object Research System Inc., Montreal, Canada) software programs.

**TEM:** The same nondemineralized specimens examined with FIB-SEM were subsequently prepared by a FIB in situ lift-out technique and studied by TEM. A Zeiss crossbeam 340 station equipped with a platinum gas injector system was utilized in this aspect of the work. Specimen areas adjacent to ROIs that were previously documented by FIB-SEM were selected for preparation. A layer of platinum, ≈1 μm thick, was initially deposited in a rectangle to protect the underlying specimen surface from ion beam damage. Trapezoidal-shaped trenches were milled on either side of the platinum deposit to a depth of ≈30–40 μm using a beam current of 15 nA. The resulting lamella was then polished with a beam current of 7 and 1.5 nA before being cut free underneath and along one side utilizing a beam current of 1.5 nA. A nanomanipulation system (Kleindiek Nanotechnik GmbH, Reutlingen, Germany) was used with a lift-out probe attached to the top of the lamella by platinum deposition. The final side of the lamella was next cut free and it was lifted out in situ. A TEM copper grid was inserted into the FIB chamber, and the lamella was attached to the side of the grid using platinum deposition. Finally, the sample was thinned to electron transparency with a series of beam currents decreasing from 100 to 50 to 20 pA. Additionally, an ultramicrotome (RMC Ultramicrotome PowerTome PT XL, Boeckeler Instruments, Inc., Tucson, AZ, USA) was also used to prepare thin sample slices for TEM analysis.

TEM was performed with a JEOL JEM-ARM200F electron microscope (JEOL, Ltd., Tokyo, Japan) operated at 200 kV and 10–15 μA, combining traditional TEM and scanning TEM (STEM). Images were obtained using both bright-field and high-angle annular dark-field detectors. An electron beam of a diameter ≈1–5 nm and dwell times of 20–200 s pixel<sup>-1</sup> were utilized in STEM mode to generate EDX spectra. Elemental maps and line profiles of specimens were collected with a JED-2300T energy-dispersive X-Ray spectrometer (JEOL) and GMS 3.4.3 Gatan microscopy suite software (Gatan, Inc., CA, USA) was used to analyze the EDX spectra.

## Supporting Information

Supporting Information is available from the Wiley Online Library or from the author.

## Acknowledgements

The authors are grateful to Aaron Chiou, Ph.D., and Claudia Fischbach, Ph.D. (Department of Biomedical Engineering, Cornell University, Ithaca, NY), and to Sarah Young, Daniela Garske and Amaia Cipitria, Ph.D. (Department of Biomaterials, Max Planck Institute of Colloids and Interfaces), for providing the mouse samples and to Holger Kropf (Helmholtz-Zentrum Berlin of Material and Energy) for TEM lamella preparation. The authors also wish to thank Clemens Schmitt, Ph.D., for technical support with FIB-SEM imaging, Daniel Werner for micro-CT imaging, Jeannette Steffen for histology staining, Birgit Schonert for sample polishing, Susann Weichold for ultramicrotome sample preparation, and Heike Runge for sample coating (all in the Department of Biomaterials at the Max Planck Institute of Colloids and Interfaces). The authors also appreciate Richard Weinkamer, Ph.D., for insightful discussion on the analysis of the connectivity of the nanochannel network.

Open Access funding enabled and organized by Projekt DEAL.

## Conflict of Interest

The authors declare no conflict of interest.

## Data Availability Statement

The data that support the findings of this study are openly available in Edmon at <https://edmond.mpdl.mpg.de/dataset.xhtml?persistentId=doi:10.17617/3.AMASWE>, reference number doi:10.17617/3.AMASWE.

## Keywords

bone, calcified cartilage, focused ion beam-scanning electron microscopy (FIB-SEM), mineralization, nanochannels

Received: December 30, 2021

Revised: March 10, 2022

Published online: April 28, 2022

- [1] B. K. Hall, *Bones and Cartilage: Developmental Skeletal Biology*, 2nd ed., MA: Academic Press 2005.
- [2] H. S. Gupta, S. Schratte, W. Tesch, P. Roschger, A. Berzlanovich, T. Schoeberl, K. Klaushofer, P. Fratzl, *J. Struct. Biol.* **2005**, *149*, 138.
- [3] T. J. Lyons, S. F. McClure, R. W. Stoddart, J. McClure, *BMC Musculoskeletal Disord.* **2006**, *7*, 52.
- [4] V. L. Ferguson, R. C. Paietta, *Structural Interfaces and Attachments in Biology* (Eds: S. Thomopoulos, V. Birman, G. M. Genin), New York: Springer, **2014**, pp. 91–118.
- [5] T. Michigami, *Ann. Pediatr. Endocrinol. Metab.* **2019**, *24*, 213.
- [6] M. D. McKee, A. Nanci, *Ann. N. Y. Acad. Sci.* **1995**, *760*, 177.
- [7] C. Hoemann, C.-H. Lafantaisie-Favreau, V. Lascau-Coman, G. Chen, J. Guzmán-Morales, *J. Knee Surg.* **2012**, *25*, 085.
- [8] T. Schar Schmidt, R. Jacquet, D. Weiner, E. Lowder, T. Schrickel, W. J. Landis, *J. Bone Surg. Am.* **2009**, *91*, 366.
- [9] R. Weinkamer, P. Kollmannsberger, P. Fratzl, *Curr. Osteoporosis Rep.* **2019**, *17*, 186.
- [10] Y. Wang, L. M. McNamara, M. B. Schaffler, S. Weinbaum, *Bioengineering, Proceedings of the Northeast Conference* Stony Brook, NY: IEEE, **2007**, Vol. 104, p. 39.
- [11] L. F. Bonewald, *J. Bone Miner. Res.* **2011**, *26*, 229.
- [12] C. W. Archer, P. Francis-West, *Int. J. Biochem. Cell Biol.* **2003**, *35*, 401.
- [13] M. D. Mayan, R. Gago-Fuentes, P. Carpintero-Fernandez, P. Fernandez-Puente, P. Filgueira-Fernandez, N. Goyanes,

- V. Valiunas, P. R. Brink, G. S. Goldberg, F. J. Blanco, *Ann. Rheum. Dis.* **2015**, *74*, 275.
- [14] D. J. Buss, N. Reznikov, M. D. McKee, *J. Struct. Biol.* **2020**, *212*, 107603.
- [15] D. M. Binkley, J. Deering, H. Yuan, A. Gourrier, K. Grandfield, *J. Struct. Biol.* **2020**, *212*, 107615.
- [16] R. M. German, P. Suri, S. J. Park, *J. Mater. Sci.* **2009**, *44*, 1.
- [17] S.-J. L. Kang, *Sintering* (Ed: S.-J. L. Kang), Oxford, UK: Butterworth-Heinemann **2005**, pp. 3–8.
- [18] H. A. Cole, M. Yuasa, G. Hawley, J. M. M. Cates, J. S. Nyman, J. G. Schoeneker, *Bone* **2013**, *52*, 337.
- [19] P. Roschger, P. Fratzl, J. Eschberger, K. Klaushofer, *Bone* **1998**, *23*, 319.
- [20] P. R. Buenzli, N. A. Sims, *Bone* **2015**, *75*, 144.
- [21] Z. Zou, T. Tang, E. Macías-Sánchez, S. Sviben, W. J. Landis, L. Bertinetti, P. Fratzl, *Proc. Natl. Acad. Sci.* **2020**, *2019*, 17932.
- [22] K. P. Arkill, C. P. Winlove, *Osteoarthritis Cartilage* **2008**, *16*, 708.
- [23] D. M. Findlay, J. S. Kuliwaba, *Bone Res.* **2016**, *4*, 16028.
- [24] C. D. DiDomenico, M. Lintz, L. J. Bonassar, *Nat. Rev. Rheumatol.* **2018**, *14*, 393.
- [25] L. Wang, *Curr. Osteoporosis Rep.* **2018**, *16*, 32.
- [26] A. Nanci, *J. Struct. Biol.* **1999**, *126*, 256.
- [27] R. T. Ingram, B. L. Clarke, L. W. Fisher, L. A. Fitzpatrick, *J. Bone Miner. Res.* **2009**, *8*, 1019.
- [28] M. D. McKee, A. Nanci, *Microsc. Res. Tech.* **1996**, *33*, 141.
- [29] O. Pullig, G. Weseloh, S. Gauer, B. Swoboda, *Matrix Biol.* **2000**, *19*, 245.
- [30] J. Luukkonen, M. Hilli, M. Nakamura, I. Ritamo, L. Valmu, K. Kauppinen, J. Tuukkanen, P. Lehenkari, *Histochem. Cell Biol.* **2019**, *151*, 475.
- [31] J. D. Currey, *Bones: Structure and Mechanics*, Vol. 2, Princeton Univ. Press, Princeton, NJ **2002**.
- [32] S. Weiner, W. Traub, H. D. Wagner, *J. Struct. Biol.* **1999**, *126*, 241.
- [33] N. Reznikov, R. Shahar, S. Weiner, *Acta Biomater.* **2014**, *10*, 3815.
- [34] A. F. van Tol, V. Schemenz, W. Wagermaier, A. Roschger, H. Razi, I. Vitiennes, P. Fratzl, B. M. Willie, R. Weinkamer, *Proc. Natl. Acad. Sci.* **2020**, *117*, 32251.
- [35] P. Kollmannsberger, M. Kerschnitzki, F. Repp, W. Wagermaier, R. Weinkamer, P. Fratzl, *New J. Phys.* **2017**, *19*, 073019.
- [36] S. van der Walt, J. L. Schönberger, J. Nunez-Iglesias, F. Boulogne, J. D. Warner, N. Yager, E. Gouillart, T. Yu, *PeerJ* **2014**, *2*, e453.
- [37] J. Nunez-Iglesias, A. J. Blanch, O. Looker, M. W. Dixon, L. Tilley, *PeerJ* **2018**, *6*, e4312.
- [38] N. Reznikov, H. Chase, Y. Ben Zvi, V. Tarle, M. Singer, V. Brumfeld, R. Shahar, S. Weiner, *Acta Biomater.* **2016**, *44*, 65.
- [39] A. Falcão, C. Feng, J. Kustra, A. Telea, *Skeletonization* (Eds: P. K. Saha, G. Borgefors, G. Sanniti di Baja), Cambridge, MA: Academic Press **2017**, pp. 43–70.
- [40] I. Zizak, P. Roschger, O. Paris, B. M. M. Misof, A. Berzlanovich, S. Bernstorff, H. Amenitsch, K. Klaushofer, P. Fratzl, *J. Struct. Biol.* **2003**, *141*, 208.
- [41] C. J. Moger, R. Barrett, P. Bleuett, D. A. Bradley, R. E. Ellis, E. M. Green, K. M. Knapp, P. Muthuvelu, C. P. Winlove, *Osteoarthritis Cartilage* **2007**, *15*, 682.
- [42] N. Reznikov, R. Almany-Magal, R. Shahar, S. Weiner, *Bone* **2013**, *52*, 676.
- [43] E. Bonucci, *Clin. Orthop. Relat. Res.* **1971**, *78*, 108.
- [44] E. Bonucci, *J. Bone Miner. Metab.* **2002**, *20*, 249.
- [45] E. Bonucci, *Mar. Drugs* **2014**, *12*, 4231.
- [46] L. Boltzmann, *Ann. Phys. Chem.* **1896**, *293*, 39.
- [47] N. Reznikov, M. Bilton, L. Lari, M. M. Stevens, R. Kröger, *Science* **2018**, *360*, eaao2189.
- [48] E. A. McNally, H. P. Schwarcz, G. A. Botton, A. L. Arsenault, *PLoS One* **2012**, *7*, e29258.
- [49] M. B. Schaffler, W.-Y. Cheung, R. Majeska, O. Kennedy, *Calcif. Tissue Int.* **2014**, *94*, 5.
- [50] H. Fleisch, R. G. G. Russell, F. Straumann, *Nature* **1966**, *212*, 901.
- [51] S. Omelon, J. Georgiou, Z. J. Henneman, L. M. Wise, B. Sukhu, T. Hunt, C. Wynnyckyj, D. Holmyard, R. Bielecki, M. D. Grynaps, *PLoS One* **2009**, *4*, e5634.
- [52] C. C. Chen, A. L. Boskey, L. C. Rosenberg, *Calcif. Tissue Int.* **1984**, *36*, 285.
- [53] A. L. Boskey, L. Spevak, S. B. Doty, L. Rosenberg, *Calcif. Tissue Int.* **1997**, *61*, 298.
- [54] K. Hoshi, S. Kemmotsu, Y. Takeuchi, N. Amizuka, H. Ozawa, *J. Bone Miner. Res.* **1999**, *14*, 273.
- [55] W. R. Thompson, S. Modla, B. J. Grindel, K. J. Czymmek, C. B. Kirn-Safran, L. Wang, R. L. Duncan, M. C. Farach-Carson, *J. Bone Miner. Res.* **2011**, *26*, 618.
- [56] E. Raguin, K. Rechav, V. Brumfeld, R. Shahar, S. Weiner, *J. Struct. Biol.* **2020**, *211*, 107530.
- [57] P. Schneider, M. Meier, R. Wepf, R. Mueller, *Bone* **2010**, *47*, 848.
- [58] E. Willbold, F. Witte, *Acta Biomater.* **2010**, 4447.
- [59] O. Behnke, T. Zelander, *J. Ultrastruct. Res.* **1970**, *31*, 424.
- [60] R. Maria, Y. Ben-Zvi, K. Rechav, E. Klein, R. Shahar, S. Weiner, *J. Struct. Biol.* **2019**, *206*, 128.
- [61] A. Boyde, F. A. Mccorkell, G. K. Taylor, R. J. Bompfrey, M. Doube, *Microsc. Res. Tech.* **2014**, *77*, 1044.